

Solder Paste Scooping Detection by Multi-Level Visual Inspection of Printed Circuit Boards

Csaba Benedek, Olivér Krammer, Mihály Janóczki and László Jakab

Abstract—In this paper we introduce an automated Bayesian visual inspection framework for Printed Circuit Board (PCB) assemblies, which is able to simultaneously deal with various shaped Circuit Elements (CE) on multiple scales. We propose a novel Hierarchical Multi Marked Point Process (H^M MPP) model for this purpose, and demonstrate its efficiency on the task of solder paste scooping detection and scoop area estimation, which are important factors regarding the strength of the joints. A global optimization process attempts to find the optimal configuration of circuit entities, considering the observed image data, prior knowledge, and interactions between the neighboring CEs. The computational requirements are kept tractable by a data driven stochastic entity generation scheme. The proposed method is evaluated on real PCB data sets containing 125 images with more than 10.000 splice entities.

Index Terms—Marked point process, PCB, scooping

I. INTRODUCTION

DEFFECT detection by Automatic Optical Inspection (AOI) is a crucial step during the manufacturing process of Printed Circuit Boards (PCB) [1], [2]. As already predicted in the late 80's [3]–[5], increasing circuit complexity, diversity of defects, economic considerations and computational requirements raise difficulties for complete PCB validation. Although AOI systems have been commonly used to recognize PCB errors [6]–[11], recent developments in resolution, quality and speed of the industrial cameras have opened several new prospects and challenges in image based verification. Earlier approaches needed to deal with compensating low image resolution by mosaicking or super resolution techniques [6]. Nowadays fine details are observable in high resolution images, which demand a hierarchical modeling approach of the PCB structure, focusing jointly on circuit regions, individual Circuit Elements (CEs), CE interactions and relevant subobject structures. This improvement enables the investigation of several previously unrecognizable features and artifacts, which can effect various phases of the manufacturing process.

Defect recognition is a strongly inter-disciplinary task, as it encapsulates problems raised by industrial technology (estimating the effects of the artifacts), optics (exploiting up-to-date imaging devices, and dealing with their limitations) and advanced vision based quality assessment [12]–[14] and pattern recognition approaches [15]–[18].

In this paper we propose a hierarchical visual inspection framework, which implements a multi-level entity extraction approach. We introduce this model suited to a selected AOI task, called scooping detection. On one hand - as introduced in the following subsection in details - scooping is a significant practical problem influencing the strength of solder joints in stencil prints. On the other hand, the relationship between the solder joints and the embedded scoops can be described by

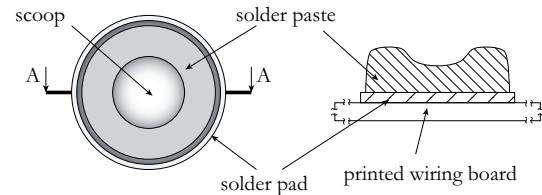


Fig. 1. Top view and side view illustrations of a solder joint with a scoop

a clear hierarchical structure, thus the methodology of the proposed approach may be adopted to various AOI tasks.

A. Production Technology Background

Nowadays reflow soldering is generally used for mechanical fastening and electrical joining of surface mounted components to electronic circuit assemblies. In mass production, at first Solder Paste (SP), which is a suspension containing powder of solder alloy and flux, is printed onto the surface of the assembly board through a metal stencil. Then components are placed onto the board into the printed paste. The third step is the formation of the joints by heating and melting - reflowing - the solder paste in conveyor type forced convection reflow ovens [19], [20].

The pitch size of integrated circuits is getting smaller and smaller and the density of components is growing as it is demanded by the continuous development of Surface Mount Technology (SMT). Consequently stencil printers and automated assembly machines are facing real challenges. Therefore to improve the quality and reliability of circuit board assemblies, the analysis of the manufacturing processes described above has a great importance. According to PCB assemblers, the quality of the printed solder pastes heavily influences the quality of solder joints. It has been reported in several studies that 52%-71% of SMT defects are related to the printing process [21]–[25]. Although other opinions keep this phase less crucial [26], it is clear that detecting earlier the printing failures may result in notable cost savings.

One major printing defect in case of small pitch-size BGA (Ball Grid Array) components is the so called scooping (see Fig. 1), when the deposited solder paste has a concave profile and its volume is less than intended based on the stencil aperture volume [27]. The scoops can also be observed in optical images taken from the PCBs (Fig. 2).

As reported by the research [28] the solder joint geometry plays an important role among the factors that can affect solder joint fatigue performance. Ball shape, standoff height, and material have effect as well on thermo-mechanical performance of BGAs and CSPs (Chip Scale Package). Previous works have demonstrated that a greater standoff height offer

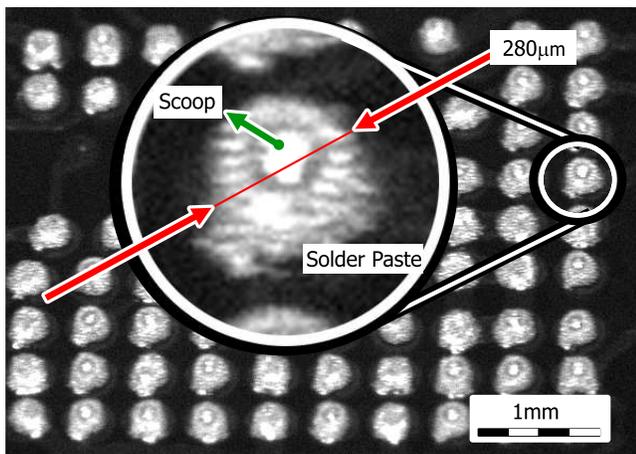


Fig. 2. 6 μm resolution image of a Printed Circuit Board, with a magnified solder paste, which contains a scoop of interest.

improved reliability performance [29] furthermore assemblies with high global thermal mismatches are necessary to have increased stand-off height to decrease the shear stress in joints during temperature changes [30]. Since the standoff-height of joints is proportional to the amount of deposited solder paste, and in this way to the degree of scooping defect, the detection of these defects has a major role to improve the quality and reliability of electronic circuit assemblies. If in the inspected PCB, the number and summarized volume of such artifacts surpass given thresholds, the board should be withdrawn. Previously, the quality of solder joints had been mostly verified by manual visual inspection [31], but as the number of components exceeds the possibilities of manual testing, reliable automation becomes a crucial need [32].

Capturing images for paste inspections is usually performed with line-scan techniques due to speed requirements. However, designing a proper source of illumination for the AOI step is a difficult issue. In addition, due to lens aberrations and limited Depth Of Field (DOF), the local contrast of the image is usually inhomogeneous depending on the Modulation Transfer Function (MTF) [33]. As a consequence, we may observe regions that exhibit defocus blur, which effect causes notable challenges for image based verification. For this reason, we integrate an optical blurring model based on the Local Contrast (LC) prior [34] into the proposed AOI method.

B. Previous AOI methods

Several methods use mathematical morphology [2], [9]–[11] as a tool for investigating geometric structures in *binary* or *grayscale* images. [9] introduces the “hit and miss transform”, which is a combination of dilation and erosion. After all, the usage of the two operations are presented in printed circuit defect detection. The method exploits prior structural evidences such as through the erosion operator one can emphasize a portion from the circuit which does not have the adequate paste thickness; or through the dilation operator we can mark out a portion from the circuit where it is not respected the distance between the feeders. [10] presented a method for segmenting binary patterns into seven mutually exclusive categories: core,

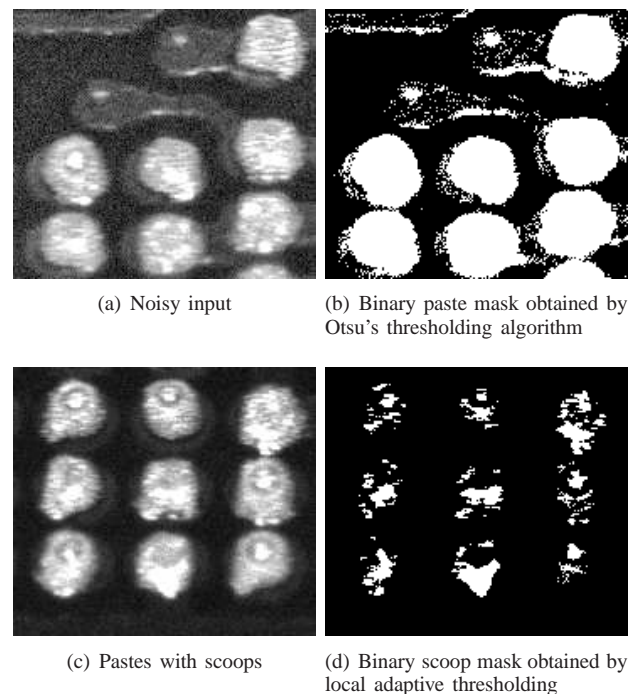


Fig. 3. Limitations of morphology based investigations. Binarized images are obtained by thresholding, optimizing the threshold for solder paste-background separation (top) and scoop center extraction (bottom). Top: in case of noisy input, separation of pastes may be inaccurate. Bottom: scoop centers can be hardly separated by thresholding

islet, loop, bridge, perforation, edge, and branch. This was achieved by applying a series of morphological transformations such as erosions, geodesic dilations, reconstruction by dilation, anchored skeletonisation, etc. The main weak point of the previously mentioned techniques is that they critically rely on the binarized image, which is usually obtained by thresholding. However estimating appropriate global or local thresholds may be difficult, as well due to local contrast defects and slight illumination variations the separation of Solder Pastes (SPs) from the background can be imperfect (see Fig. 3(a)-(b)). As shown in [35], even with applying efficient locally adaptive binarization algorithms [36], fine structures, such as scoops, can be hardly separated from binarized images (Fig. 3(c)-(d)).

An alternative solution could be applying *grayscale* morphological operations [37], or traditional segmentation-based approaches [38], [39]. However, PCB images often contain oversaturated regions, which concern both scoop centers and other SP parts as well, whose separation is hence not possible based on purely intensity or micro-textural properties of the observed optical data. While segmentation techniques may efficiently separate ‘background’ areas on the boards from large component packages such as Integrated Circuits (ICs) or connectors; and from strongly textured regions containing *groups* of small resistors, transistors or capacitors; they can be less efficient, if we attempt to describe the boards at the CE-object level, having strong prior information about the geometry of the entities. We have also tested classical image processing techniques such as the Hough transform based

ellipse detection, and the *Watershed* segmentation [39], but we found them inefficient for the scooping detection problem.

The quality control task is often interpreted as a change detection problem. [1] presents a system to inspect metal stencil that is used to print solder paste on pads of PCBs. In [11], defects in tested PCBs are identified by feature comparison between the detected images and template images based on a linkage information table. Similar comparison-based approach is reported in [40], where the major components of the PCB inspection system consist of image alignment and defect detection using Hausdorff distance based matching to a reference image, while defect classification is obtained by a support vector machine. However, the previous change based approaches face also a few difficulties. Firstly, image alignment may mean bottleneck of the whole verification process, if the matched features are weak and cannot be reliably detected [40]–[42]. Secondly some artifacts result in typical structural patterns rather than typical changes - as bright or dark mutations of solder paste regions do not indicate scoops in general (see Fig. 3(c)). In this case template or pattern matching is preferred [43].

Marked Point Processes (MPP) [44] provide efficient tools to extend conventional Markov Random Field (MRF, [45]) based pixel level classification techniques, by taking into account the geometry in the proposed models. An MPP model works with objects as variables rather than with pixels, so that the number of variables is also unknown. Moreover, similarly to MRFs, MPPs can also embed prior constraints and data models within a global configuration probability function, and various techniques for optimizing the models [46], [47] and estimating the parameters [48] are available. However, implementing a multi-level PCB inspection task is challenging in the MPP framework. For comparison, in a basic MPP solution [47], flamingo populations are investigated in aerial images, where all birds are modeled by ellipses with similar sizes. In that case, model optimization can be efficiently performed by applying randomized object birth-death moves after coarse estimation of the object centers. Conversely, to cope with our addressed problem, we have to deal with a couple of difficulties:

- *Hierarchy*: PCB elements appear at multiple hierarchical levels, e.g. Solder Pastes (SPs) and included scoops.
- *Heterogeneity*: SPs have various geometric shapes.
- *Multi-scaling*: SP sizes are in different orders of magnitudes.

For these reasons, we introduce here a new *Hierarchical Multi Marked Point Process* (H^M MPP) model with the following three key properties:

(i) We describe the hierarchy between objects and object parts as a parent-child relationship embedded into the MPP framework. The proposed schema extends the approach used in our earlier models [35], [49], so that we consider here both data based and prior features in multi-level entity connection modeling.

(ii) To simultaneously deal with variously shaped circuit elements, we jointly sample different types of geometric objects, by adopting the multi-marked point process schema [50] to the hierarchical entity extraction problem. From the

TABLE I
METHODOLOGICAL OVERVIEW ON MPP METHODS (\checkmark =YES, \times =NO).

Reference method	Hierarchy		Multi MPP	Bottom-Up Samp.	
	Prior	Data		Prior	Data
PAMI-08 [46]	\times	\times	\times	\times	\times
MIV-09 [47]	\times	\times	\times	\times	\checkmark
PAMI-10 [50]	\times	\times	\checkmark	\times	\times
PAMI-11 [18]	\times	\times	\times	\times	\checkmark
PRL-11 [35]	\checkmark	\times	\times	\times	\times
H^M MPP	\checkmark	\checkmark	\checkmark	\checkmark	\checkmark

point of view of the end-user, the H^M MPP model significantly generalizes [35], where purely ellipse shaped elements have been investigated.

(iii) To efficiently sample the SP population space, we develop a Bottom-Up (BU) stochastic object proposal strategy, by combining low level statistical image descriptors [18], [51] with prior information based structure estimation. This step keeps the computational complexity tractable, although due to properties (i) and (ii) the dimension and size of the solution space are significantly increased.

The proposed H^M MPP model also has methodological contribution over various earlier MPP approaches, as shown by Table I. Note that in our earlier published methods [35], [49], we have only partially addressed the task (i), while challenges in (ii) and (iii) have been completely ignored there. On the other hand, the further reference techniques [18], [46], [47], [50] deal with significantly different application domains, thus they do not address specific challenges of AOI problems.

II. PROBLEM FORMULATION

The input of the proposed method is an optical image taken from a PCB with printed Solder Pastes (SP). The goal is to detect and separate the SPs, and simultaneously extract the scoop artifacts, which may appear in some pastes (Fig. 2). We approximate the shape of the SPs by various plane figures from a shape library, in this paper ellipses (\circ), rectangles (\square) and isosceles triangles (\triangle) are used. On the other hand, we model a Scoop Object (SO) by two concentric ellipses as it consists of a bright central region (inside the internal ellipse) and a relatively darker elliptical ring (region between the internal and external ellipses) enclosed by the brighter SP patch (see Fig. 4). In several cases the separation is not trivial due to weak contrast (see Fig. 16).

Let us denote by S the pixel lattice of the input image and by $s \in S$ a single pixel. G refers to the observed grayscale image. Let u be a SP object candidate of the board, whose shape is defined by its *shape type* attribute $tp(u) \in \{\circ, \square, \triangle\}$. For each object, we define the coordinates of a reference point $o = [o_x, o_y]$, the orientation $\theta \in [-90^\circ, +90^\circ]$, and the geometry is described by a_M and a_m length parameters, which are the major and minor axes for ellipses, the perpendicular side lengths for rectangles, and a side-altitude pair for triangles (see details in Fig. 4). In addition, each SP may contain child object $q_u \in \{\{\text{nil}\} \cup Q\}$, while $q_u = \text{nil}$ denotes no scooping in u . A SO object q lives in the Q parameter space, which is determined by the c_x, c_y center coordinates, b_M and b_m semi-axes of the internal ellipses; d_M and d_m ring with parameters

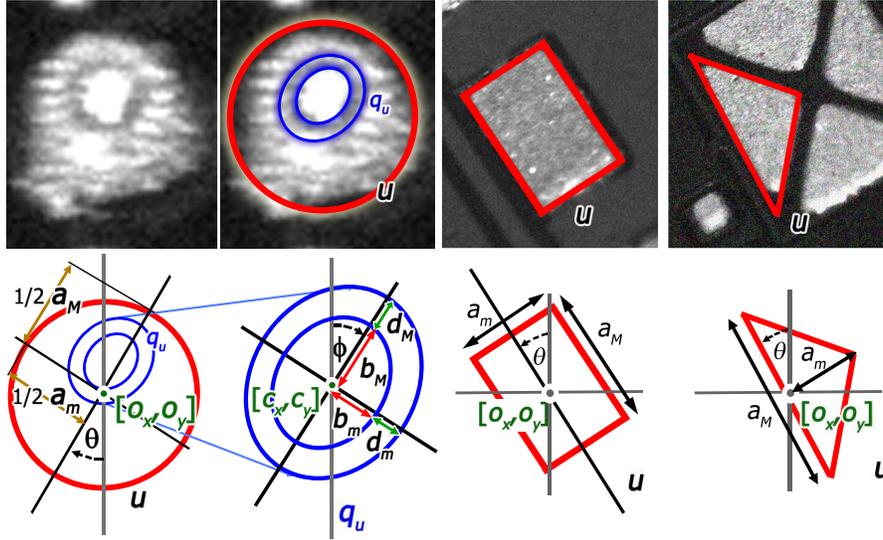


Fig. 4. Notations of the elliptical model of a Solder Joint and the bi-elliptical scooping effect

so that the axes of the external ellipse are $b_M + d_M$ and $b_m + d_m$, respectively. ϕ denotes the orientation of the SO.

Let us denote the set of all the possible u SP objects by \mathcal{H} . The Ω configuration space is defined as [47]:

$$\Omega = \bigcup_{n=0}^{\infty} \Omega_n, \quad \Omega_n = \{\{u_1, \dots, u_n\} \in \mathcal{H}^n\}$$

Denote by ω a given object configuration $\{u_1, \dots, u_n\}$ in Ω .

III. HIERARCHICAL MULTI MARKED POINT PROCESS MODEL

We describe the configuration of the Solder Pastes and the included Scoop Objects with a novel *Hierarchical Multi Marked Point Process Model*. First, we introduce a non-homogeneous data-dependent Gibbs distribution on the Ω configuration space: $P(\omega) = 1/Z \cdot \exp[-\Phi(\omega)]$, where $\Phi(\omega)$ is called the configuration energy and Z is a normalizing constant. The $\Phi(\omega)$ energy function is a composition of a data term, $\Phi_d(\omega)$, which measures how the configuration fits the observed image data; and a prior term, $\Phi_p(\omega)$, which takes into account geometric interactions between the objects:

$$\Phi(\omega) = \Phi_p(\omega) + \nu \cdot \Phi_d(\omega) \quad (1)$$

where ν is a positive weighting factor.

The optimal SP population $\hat{\omega}$ is obtained as the Maximum Likelihood (ML) configuration estimate based on the $P(\omega)$ density:

$$\omega_{\text{ML}} = \underset{\omega \in \Omega}{\operatorname{argmax}} P(\omega) = \underset{\omega \in \Omega}{\operatorname{argmin}} \Phi(\omega). \quad (2)$$

To fit the above framework to the SP detection task, we need construct an appropriate $\Phi(\omega)$ energy function, so that the ML configuration efficiently estimates the true SP population. For this reason, we dedicate the rest of this section to the definition of the *data* and *prior* energy terms.

A. Data Energy

We assign to each object u a data-dependent energy term $\varphi_d(u)$, which evaluates u depending on the local image data, but independently of other objects of the configuration. Then, the data term of the population is calculated as:

$$\Phi_d(\omega) = \sum_{u \in \omega} \varphi_d(u) \quad (3)$$

A SP u with $\varphi_d(u) < 0$ is called *attractive object*, since according to (3) adding attractive objects to the population may decrease the global configuration energy.

The $\varphi_d(u)$ function is decomposed into a parent term $\varphi_d^p(u)$ and a child term $\varphi_d^c(u, q_u)$. In the obtained circuit images the *parent* Solder Pastes appear as bright ellipses surrounded by darker background. To evaluate the contrast between the SPs and the board, we calculate the Bhattacharya [47] distance $d_B(u)$ between the pixel intensity distributions of the internal SP regions and their boundaries:

$$d_B(u) = 1 - \sum_i \sqrt{\lambda_u^{\text{in}}(x_i) \cdot \lambda_u^{\text{out}}(x_i)}$$

where $\lambda_u^{\text{in}}(x)$ (resp. $\lambda_u^{\text{out}}(x)$) is the empirical gray level distribution of the pixels belonging to u (resp. a concentric elliptical ring around u), and x_i $i = 1, \dots, K$ are discrete gray levels of the histogram bins, shown in Fig. 5.

In the next step, we construct the parent energy term, so that we attempt to satisfy $\varphi_d^p(u) < 0$ for real SPs and $\varphi_d^p(u) \geq 0$ for false candidates. For this purpose, we project the Bhattacharya feature domain to $[-1, 1]$ with a monotonously decreasing Q function (see also Fig. 5):

$$\begin{aligned} \varphi_d^p(u) &= Q(d_B(u), d_0) = \\ &= \begin{cases} \left(1 - \frac{d_B(u)}{d_0}\right) & \text{if } d_B(u) < d_0 \\ \exp\left(-\frac{d_B(u) - d_0}{10}\right) - 1 & \text{if } d_B(u) \geq d_0 \end{cases} \quad (4) \end{aligned}$$

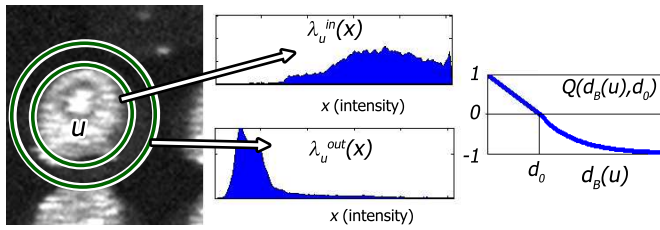


Fig. 5. Utility of the $\lambda_u^{\text{in}}(x)$ and $\lambda_u^{\text{out}}(x)$ histograms for the parent data term calculation

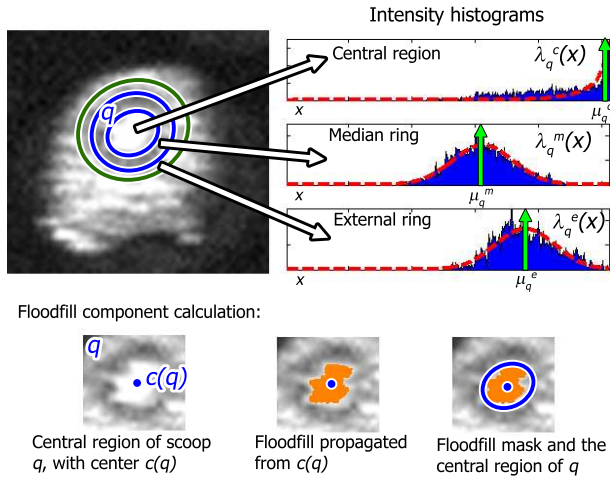


Fig. 6. Child data term calculation. Top: intensity histograms, bottom: floodfill feature demonstration

where the d_0 parameter is set based on training regions [18]. As shown in Fig. 5, object u is attractive according to the $\varphi_d^p(u)$ term iff $d_B(u) > d_0$.

The construction of the *child's data term* $\varphi_d^c(u, q_u)$ needs more complex investigations. We use $\varphi_d^c(u, \text{nil}) = 0$, otherwise we distinguish three regions of each scoop: the central bright ellipse, the darker median ring and the bright external ring, as shown in Fig. 6. Experimental evidences prove, that for a real scoop q , the gray level histogram of the central region, $\lambda_q^c(x)$ follows a skewed distribution, which can be approximated by a Beta density function (shown with dashed line in Fig 6 in the top). Similarly, the medium and external

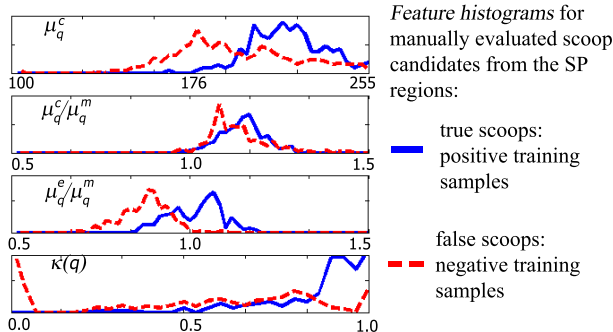


Fig. 7. Histogram of child data features obtained from manually evaluated true and false scoop candidates.

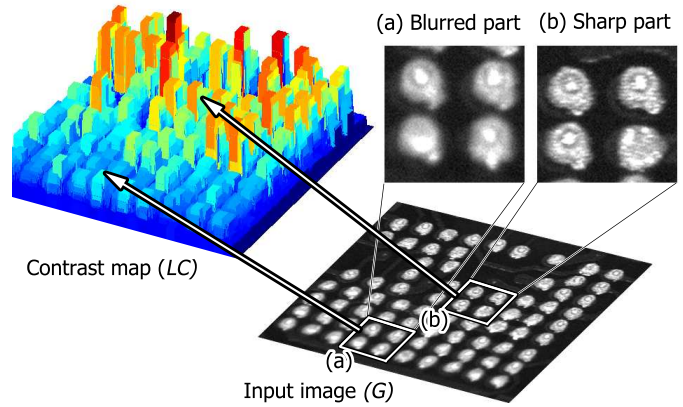


Fig. 8. Contrast map demonstration

region histograms ($\lambda_q^m(x)$ resp. $\lambda_q^e(x)$) can be approximated by Gaussian densities. On the other hand, the scoop center region is a usually compact bright blob, and if we apply a floodfill propagation from the central point $c(q)$, the flooded region does not hang over the internal ellipse significantly (Fig 6 bottom). To avoid errors caused by narrow bright connections between the scoop center and further bright SP parts, we apply the floodfill step for the input image undergone a grayscale erosion filter.

Let us denote by μ_q^c the peak location of $\lambda_q^c(x)$, and by μ_q^m resp. μ_q^e the empirical mean values of the $\lambda_q^m(x)$ resp. $\lambda_q^e(x)$ distributions. We characterize a scoop candidate by the following four features:

- (i) μ_q^c : dominant brightness value of the central region
- (ii) intensity ratio μ_q^c / μ_q^m : contrast between the central region and median ring
- (iii) intensity ratio μ_q^e / μ_q^m : contrast between the external ring and median ring
- (iv) $\kappa(q) = \frac{F^c}{T^c} \cdot (1 - \frac{F^m}{T^m})$: feature obtained by floodfill propagation from $c(q)$. T^c and T^m mark the area of the central region resp. median ring, F^c and F^m denote the flooded area of the corresponding regions.

For a statistical analysis of the above descriptors, we have collected Ground Truth SOs and false candidates from training images, and compared the feature histograms of the positive and negative samples (see Fig. 7). The noticeable differences between the matched distributions confirm that the extracted features provide valuable information for SO separation. However, since the histograms are overlapping in the individual feature dimensions, a joint consideration of the descriptors is necessary for correct classification.

The sketch of the proposed feature integration process is the following. First we assign to each descriptor an energy term using the Q -function similarly to (4), so that we set the d_0 acceptance threshold parameter as *low*, as the attractive region of Q involves almost the complete feature domain of the positive training objects. To decrease the number of false alarms, we prescribe that for a real scoop, the (i)-(iv) features should be simultaneously appropriate. Therefore, the child's data-energy value is calculated using the averaging and the maximum operators (latter one is equivalent to the logical AND in the negative fitness domain) from the subterms of the

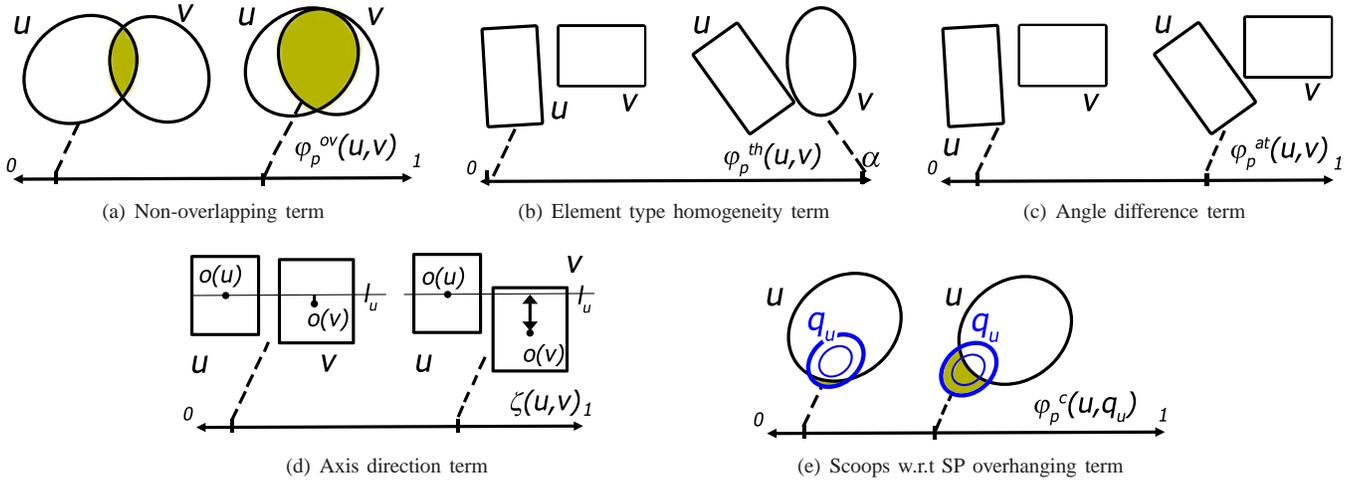


Fig. 9. Calculation of the prior terms. Constraints (a)-(d) implement various SP level interactions, (e) influences the relation of SPs and included SOs

four constraints. Since as detailed before, the contrast of the PCB images may be notably inhomogeneous (see also Fig. 8), the acceptance threshold for the intensity ratios μ_q^c/μ_q^m , μ_q^e/μ_q^m should also vary over the S pixel lattice. To characterize the local sharpness of the image, we calculate a contrast dependent term, $\xi(u)$, which is estimated by the mean Local Contrast (LC) prior value of the parent SP's (u) image region [34]:

$$\xi(u) = \sum_{s \in u} LC(s)$$

using the following contrast definition (see also Fig. 8):

$$LC(s) = \frac{\max_{r \in W_l(r)} \nabla G(r)}{\max_{r \in W_l(r)} G(r) - \min_{r \in W_l(r)} G(r)}$$

where $W_l(r)$ is a $l \times l$ rectangular window around pixel r and ∇G is the gradient image.

Finally, the complete data energy term for a given scoop candidate is derived as:

$$\varphi_d^c(u, q_u) = \max \left(\frac{1}{2} Q(\mu_{q_u}^c, d^c) + \frac{1}{2} Q(\kappa(q_u), d^{\kappa}), \right. \\ \left. Q(\mu_{q_u}^c / \mu_{q_u}^m, \xi(u) \cdot d^{\text{cm}}), \right. \\ \left. Q(\mu_{q_u}^e / \mu_{q_u}^m, \xi(u) \cdot d^{\text{em}}) \right) \quad (5)$$

Free parameters of the scoop model are d^c , d_{κ} , d^{cm} and d^{em} , which should be set based on training data (Sec. V).

With summarizing the parent and child terms, the data energy of the SP candidate u is obtained as

$$\varphi_d(u) = \varphi_d^p(u) + \varphi_d^c(u, q_u)$$

B. Prior Energy

In contrast to the data-energy model, the $\Phi_p(\omega)$ term evaluates a given configuration on the basis of prior geometric constraints. We used four types of prior terms in the model, implementing *non-overlapping*, *type homogeneity*, and *alignment* constraints between different SPs, and the *scoop encapsulation* constraint between a SP and its child SO.

1) *Non-overlapping*: Since we aim to extract individual SP entities, we must penalize overlapping between different SP objects. Thus, we define first a $\overset{\text{int}}{\sim}$ intersection relation in \mathcal{H} , so that for a given (u, v) SP pair $u \overset{\text{int}}{\sim} v$ holds, iff their geometrical figures intersect. Then, the energy term of the *non-overlapping* constraint $\varphi_p^{\text{ov}}(u, v)$ is defined for each $u \overset{\text{int}}{\sim} v$ object pair, and it is calculated as the normalized overlapping area (see Fig. 9(a)):

$$\varphi_p^{\text{ov}}(u, v) = \frac{\#\{s | s \in u, s \in v\}}{\#\{s | s \in u\} + \#\{s | s \in v\}}$$

where $s \in u$ means that pixel s is covered by object u , and $\#$ refers to the cardinality of a set.

2) *Element type homogeneity*: In PCBs we can often observe that several SPs with the same type form spatially connected groups. Relying on this prior assumption, we should favor SP configurations, where the neighboring entities have mostly identical types which can be expressed by the Potts constraint [52].

We define here a $\overset{\text{nb}}{\sim}$ neighborhood relation, where $u \overset{\text{nb}}{\sim} v$ iff the distance of their geometric figures is lower than a distance threshold. For the management of this neighborhood, a regular grid is projected to the image, which divides it into rectangular regions, called *paving cells*. Then, each SP candidate is registered to the intersecting paving cells, so that pointers are maintained in both direction between the corresponding cells and the circuit objects. In this way, the neighborhood of each SP can be efficiently determined.

Based on the previously defined neighborhood, the *type homogeneity* energy term is obtained as:

$$\varphi_p^{\text{th}}(u, v) = \begin{cases} 0 & \text{if } \text{tp}(u) = \text{tp}(v) \\ \alpha & \text{if } \text{tp}(u) \neq \text{tp}(v) \end{cases} \quad (6)$$

with an $\alpha > 0$ constant.

3) *Alignment*: SPs in the printed boards are usually aligned, i.e. most of the neighboring entity pairs are either parallel or perpendicular. Considering this prior feature, we can also prescribe on the previously defined $\overset{\text{nb}}{\sim}$ neighborhood two

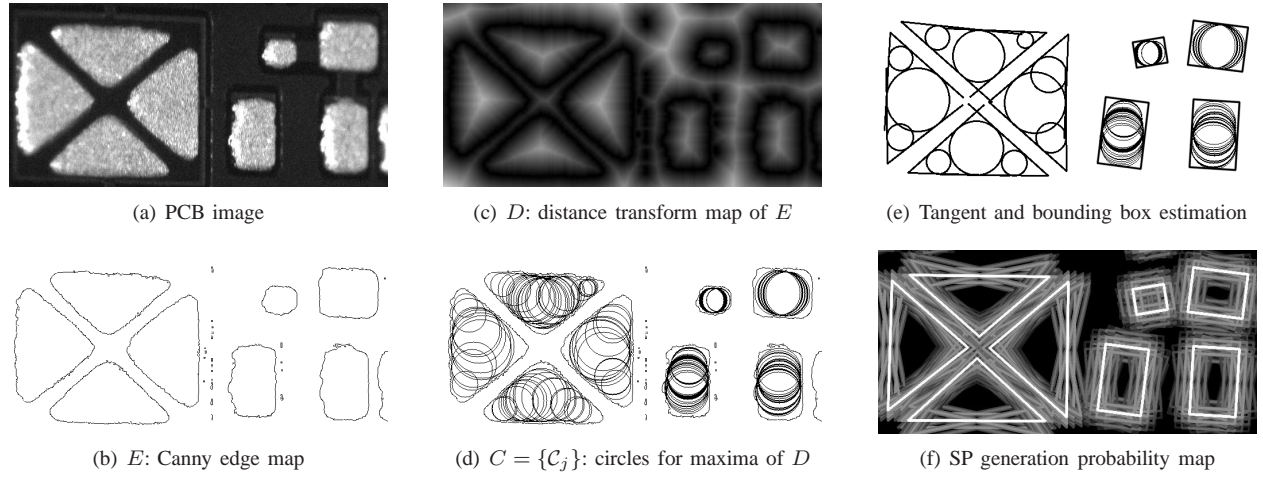
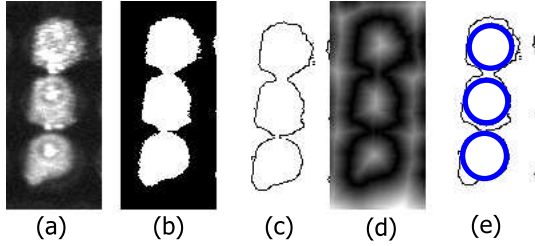


Fig. 10. Steps of the bottom-up entity proposal process


 Fig. 11. Demonstration of the preliminary detection results for touching SPs. (a) input image part (b) coarse binary SP mask (c) E edge map (d) D distance map (e) initial SP candidates (circles)

alignment condition terms. The first one penalizes the angle difference (ad) between the neighboring entities (Fig. 9(c)):

$$\varphi_p^{\text{ad}}(u, v) = \gamma^{\text{ad}} \cdot \Lambda(|\theta(u) - \theta(v)| \bmod 90^\circ)$$

where $u \overset{\text{nb}}{\sim} v$ and $\Lambda(x)$ is a tent function:

$$\Lambda(x) = 1 - \frac{|45^\circ - x|}{45^\circ}, \quad x \in [0, 90^\circ]$$

Using the above term, SPs will be favored, which have in average similar orientation to *most of their neighbors*. On the other hand, we also prescribe another strict alignment constraint: we expect that in the neighborhood of each SP u there exists *at least one* SP v , so that the central point of v (denoted by $o(v)$) is close to one of the main axis lines of u (l_u). The corresponding energy term is obtained as:

$$\varphi_p^{\text{at}}(u, \omega) = \min_{v: u \overset{\text{nb}}{\sim} v} \zeta_d(u, v)$$

where $\zeta_d(u, v) = (\zeta(u, v) + \zeta(v, u))/2$ and $\zeta(u, v)$ is the normalized distance of l_u and $o(v)$ as shown in Fig. 9(d).

4) *Scoop Encapsulation*: While previous prior terms prescribe soft constraints between SP objects, we define the *Encapsulation* condition between a given SP and its included scoop. Here penalize if a scoop q_u overhangs its parent paste u , which is measured by the $\varphi_p^{\text{se}}(u, q_u)$ overhanging area normalized by the area of the scoop (see Fig. 9(e)):

$$\varphi_p^{\text{se}}(u, q_u) = \frac{\#\{s | s \in q_u, s \notin u\}}{\#\{s | s \in q_u\}}$$

By definition, we use $\varphi_p^{\text{se}}(u, \text{nil}) = 0$.

In the development phase of the model, we have tested a couple of fusion formulas to derive the joint prior energy term from the above subterms. We found here that the summarization is more efficient than the maximum operator (later one was used for the data term construction): by adding the prior terms, we do not strictly prescribe the simultaneous fulfillment of all prior constraints, although we prefer low energies regarding the individual components. Therefore, the complete prior energy term of the population is calculated as:

$$\begin{aligned} \Phi_p(\omega) = & \sum_{u \overset{\text{int}}{\sim} v} \varphi_p^{\text{ov}}(u, v) + \sum_{u \overset{\text{ng}}{\sim} v} \varphi_p^{\text{th}}(u, v) + \sum_{u \overset{\text{ng}}{\sim} v} \varphi_p^{\text{ad}}(u, v) \\ & + \sum_{u \in \omega} \varphi_p^{\text{at}}(u, \omega) + \sum_{u \in \omega} \varphi_p^{\text{se}}(u, q_u) \end{aligned} \quad (7)$$

IV. OPTIMIZATION

The previously introduced prior and data dependent potential terms define the $\Phi(\omega)$ configuration energy completely, however, finding the optimal ω_{ML} object population needs to perform an efficient search in the high dimension population space, where local maxima of the energy function can mislead the optimization. Due to time and quality constraints of the manufacturing process, the computational efficiency and detection performance of the optimization plays a particularly crucial role in the addressed application. We can find an extensive bibliography for MPP energy minimization. Most previous approaches use the iterative Reversible Jump Markov Chain Monte Carlo (RJCMCMC) scheme [46], [50], where each iteration consists in perturbing one or a couple of objects (e.g. SPs) using various kernels such as birth, death, translation, rotation or dilation. Here experiments show that the rejection rate, especially for the birth move, may induce a heavy computation time. Besides, one should decrease the temperature slowly, because at low temperature, it is difficult to add objects to the population.

A recent alternative approach, called the Multiple Birth and Death Dynamic technique (MBD) [47] evolves the population

of objects by alternating purely stochastic object generation (*birth*) and removal (*death*) steps, in a Simulated Annealing (SA) framework. In contrast to the above mentioned RJMCMC implementations, each birth step of MBD consists of adding several random objects to the current configuration, and there is no rejection during the birth step, therefore high energetic objects can still be added independently of the temperature parameter. Due to these properties, in several tasks notable gain has been reported in optimization speed versus RJMCMC [18], [47], [53]. However, in these previous models the dimension and extension of the object parameter space is relatively small. Conversely, the proposed H^MMPP model must deal with variously shaped and scaled circuit elements, while the embedded SOs increase onwards the dimension of the object descriptor vector. As a comprise, we supplement the MBD algorithm with three simple moves: shape perturbation, type change and child maintenance, so that the optimization in the multidimensional parameter space is decomposed to computationally efficient steps. On the other hand, instead of applying fully random sampling, we construct a data driven stochastic entity generation scheme, which proposes relevant SPs with higher probability based on various image features. This approach uses a similar idea to the Data Driven MCMC scheme [51] or to the birth maps in [18], [47], however we extend here the bottom-up parameter estimation process for all descriptors (location, orientation and shape) of the circuit elements.

The goal of the *Bottom-Up Stochastic Entity Proposal* process is to assign to the different image pixels (1) pseudo probability values that the pixel is an object reference point (e.g. center of an ellipse) (2) narrow distributions for object parameters expected in the given pixels. In this way the entity proposal maintains the reversibility of the iterative evolution process of the SP population [51], instead of implementing a greedy algorithm. On the other hand, this bottom up-process can efficiently guide the object exploration step towards efficient candidates. We use in the preprocessing step a binary *foreground* mask B obtained by Otsu's thresholding method from the input image, which realizes a coarse separation of the circuit entities (ie. foreground) from the board (ie. background). However, due to notable noise (as in Fig. 3(b)), this B mask can be unreliable for purposes of SP separation and shape estimation. In addition, some neighboring SPs may also be merged into one blob in the mask (Fig 11(b)). The steps of the *SP Candidate Generation* process are shown in Fig. 12 (see also Fig 10). Thereafter, we have to separately deal with the *R&E* (rectangle or ellipse) and the *Triangle candidates* in the following ways:

R&E candidates: for each object, we estimate the bounding rectangle \mathcal{R} of the union of the corresponding circles (Fig. 10(e), right). Let us assume that we have detected n_r R&E object candidates: $\{\mathcal{R}_1, \dots, \mathcal{R}_{n_r}\}$ and let $o(\mathcal{R}_i)$ be the center of \mathcal{R}_i . Then, for each pixel s , we determine the closest rectangle $\mathcal{R}_s^{\min} = \operatorname{argmin}_i \|s - o(\mathcal{R}_i)\|$ and calculate the birth value:

$$P_b^{\mathcal{R}}(s) = k_{\mathcal{R}} \left(\frac{\|s - o(\mathcal{R}_s^{\min})\|}{h_{\mathcal{R}}} \right) \quad (8)$$

with a $k_{\mathcal{R}}(\cdot)$ kernel function, and $h_{\mathcal{R}}$ bandwidth parameter

Algorithm: SP Candidate Generation

Step 1. Generate the Canny edge map E of the PCB image (Fig. 10(b))

Step 2. Generate the distance transform map of E , and denote it by D (Fig. 10(c))

Step 3. Find local maxima pixels in D : $\{s_{\text{lx}}^i | i = 1, 2, \dots, n_{\text{lx}}\}$, and for each i draw a \mathcal{C} circle with center s_{lx}^i and radius $D(s_{\text{lx}}^i)$. Keep only circles which correspond in majority to foreground regions of the coarse B foreground mask: $C = \{\mathcal{C}_j | j = 1, \dots, n_c\}$. We denote henceforward by $\mathcal{C}_j \stackrel{\text{int}}{\sim} \mathcal{C}_i$ if \mathcal{C}_j and \mathcal{C}_i circles intersect (Fig. 10(d)).

Step 4. We define an indirect intersection relation $\stackrel{i\mathcal{C}'}{\sim}$ for a subset $\mathcal{C}' \subset \mathcal{C}$ where for each $\mathcal{C}_j, \mathcal{C}_i \in \mathcal{C}'$: $\mathcal{C}_j \stackrel{i\mathcal{C}'}{\sim} \mathcal{C}_i$ iff $\mathcal{C}_j \stackrel{\text{int}}{\sim} \mathcal{C}_i$ or $\exists \mathcal{C}_k \in \mathcal{C}': \mathcal{C}_j \stackrel{\text{int}}{\sim} \mathcal{C}_k$ AND $\mathcal{C}_k \stackrel{i\mathcal{C}'}{\sim} \mathcal{C}_i$

Step 5. We prepare an n -partition of $\mathcal{C} = \mathcal{C}_1 \cup \mathcal{C}_2 \cup \dots \cup \mathcal{C}_n$ so that for each l each $\mathcal{C}_j \in \mathcal{C}_l$ is in $\stackrel{i\mathcal{C}_l}{\sim}$ relation with all elements in \mathcal{C}_l , but not with any other circles from $\mathcal{C} \setminus \mathcal{C}_l$ (see in Fig. 10(d) the grouped circles).

Step 6. To all partitions obtained above we assign a SP candidate. For each \mathcal{C}_l we calculate the radius-variation of the included circles. If the variation is high enough we mark the object as a *triangle* candidate, otherwise as a *R&E* (rectangle or ellipse) candidate. Choice between rectangles and ellipses will only be made in the consecutive optimization step (Fig. 13), based on data dependent and prior features of proposed candidates.

Fig. 12. Pseudo code of the SP Candidate Generation algorithm, used in the *Bottom-Up Stochastic Entity Proposal* process of the HMBD optimization

[18]. Besides marking the candidate regions of the rectangular or elliptical SP centers, the $\{\mathcal{R}_i | i = 1 \dots n_r\}$ set provides local estimations for the side/axis length and orientation parameters: $\mu_M^{\mathcal{R}}(s) = a_M(\mathcal{R}_s^{\min})$, $\mu_m^{\mathcal{R}}(s) = a_m(\mathcal{R}_s^{\min})$ and $\mu_\theta^{\mathcal{R}}(s) = \theta(\mathcal{R}_s^{\min})$.

Triangle candidates: determine the circles with the minimal and maximal radius of the group, and the circle which has the highest distance from the minimal circle (Fig. 10(e), left part). Calculate joint tangents of the maximal and minimal circles. Estimate the triangle sides accordingly. Let us assume that we have detected n_t triangle candidates: $\{\mathcal{T}_1, \dots, \mathcal{T}_{n_t}\}$, and similarly to the R&E case, we derive here a triangle birth map $P_b^{\mathcal{T}}(\cdot)$ with estimated side length and orientation values $\mu_M^{\mathcal{T}}(\cdot)$, $\mu_m^{\mathcal{T}}(\cdot)$ and $\mu_\theta^{\mathcal{T}}(\cdot)$.

Finally the detailed pseudo code of the HMBD algorithm can be followed in Fig. 13.

V. PARAMETER SETTINGS

We can divide the parameters of the proposed H^MMPP technique into three groups corresponding to the *prior model*, *data model* and the *MBD optimization*.

The parameters of the *prior* and *data* terms are set based on manually evaluated training data. We can follow the supervised approach, since for most AOI systems, the illumination, image contrast, element type and size, and expected error characteristic can be considered constant during the inspections, which makes possible to calibrate the parameters in the system initialization phase. Relevant prior term parameters are the ν

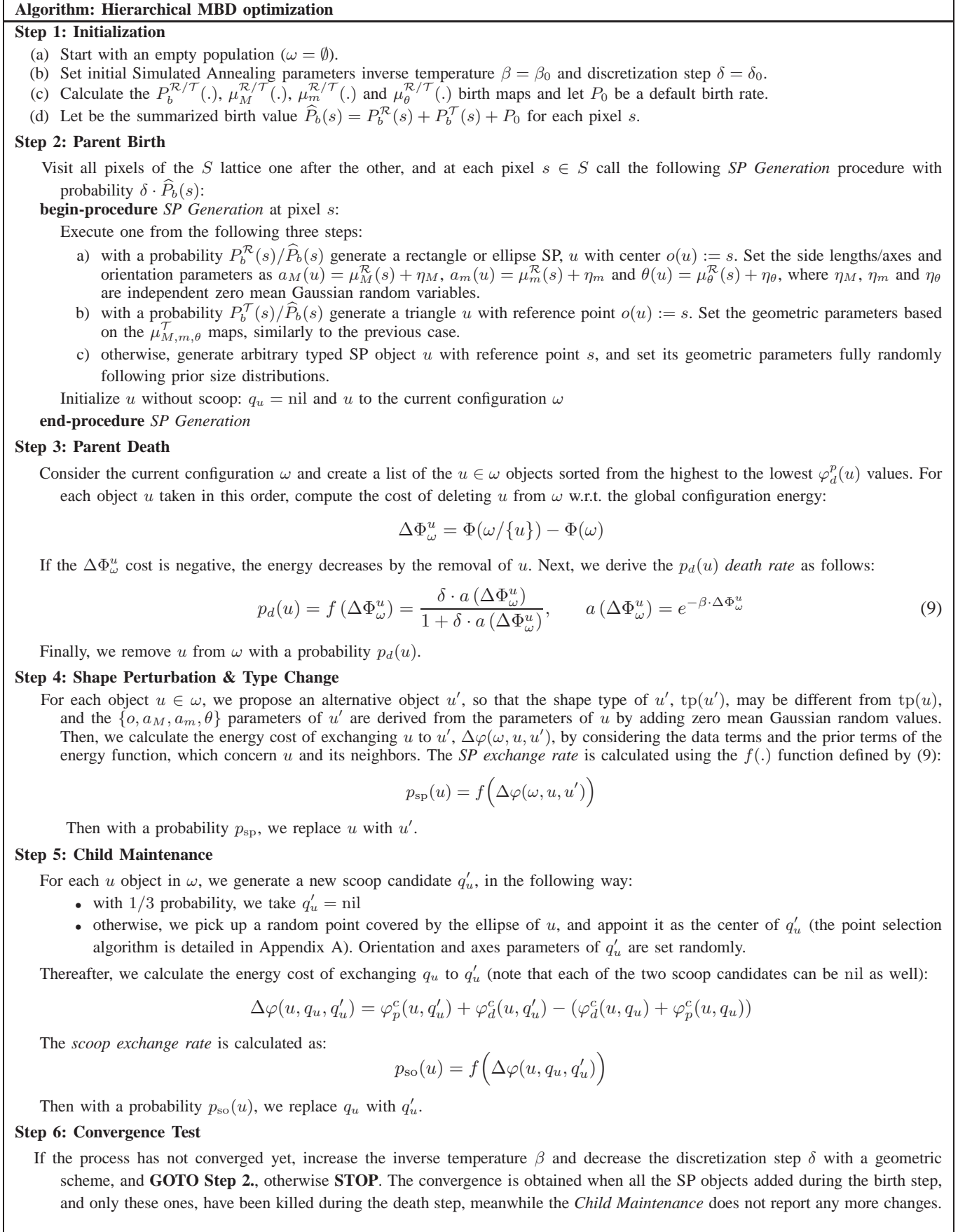


Fig. 13. Pseudo code of the developed Hierarchical Multiple Birth and Death optimization algorithm

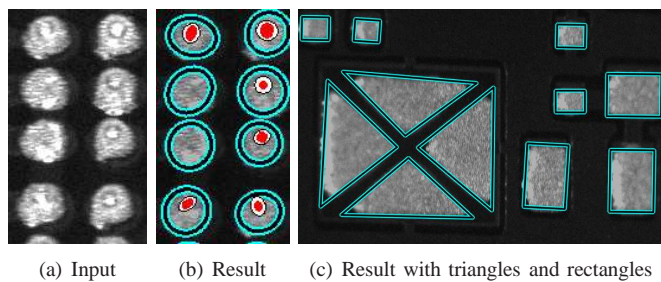


Fig. 14. H^M MPP result: extracting variously shaped circuit elements, detected scoops are shown by filled concentric ellipses in (b)

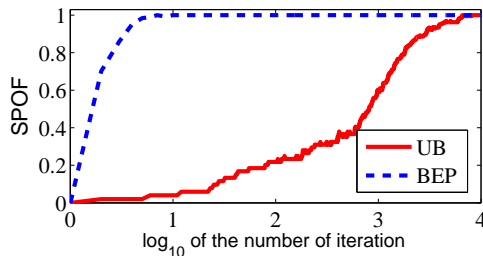


Fig. 15. Evolution of the detection performance over the iteration steps during the optimization on a selected test image from the SetHeavy image set. Solder Paste Object-level F-rate (SPOF) is given as a function of the logarithm of the applied birth steps.

weighting factor in (1), and the α and γ^{ad} weights of different prior term components. To define the data term, we should fix d_0 , d^c , d^r , d^{em} and d^{em} , the window size used for calculating the LC prior, and the width of object boundaries for calculating $d_B(u)$ and $\lambda_q^e(\cdot)$. For setting all of these coefficients, one can take a Maximum Likelihood Estimator (MLE), details can be found in [48]. Finally, regarding the *relaxation* parameters, we followed the guidelines provided in [47] and used $\delta_0 = 10000$, $\beta_0 = 20$ and geometric cooling factors $1/0.96$.

VI. EXPERIMENTS

A. Experiment configuration

We have tested the proposed model on a three real PCB datasets, whose main properties are summarized in Table II. SetHeavy contains 44 images with *heavy* scooping ratio of 14% (664 scoops in 4655 SPs), while SetSparse includes similar PCB photos, with a much lower SO rate of 3% (112 scoops out of 4100 pastes in 66 images). In the third collection, SetDark (1283 pastes in 12 images), the scooping artifact does not appear at all, however, due to lower image quality the accurate SP extraction step is more challenging. The circuits contain variously shaped Solder Pastes, in particularly elliptical, rectangular and triangular elements. Also the scales of the different SPs show a large variety: side length/diameter values vary from $250\mu\text{m}$ to $2000\mu\text{m}$. The elliptical solder pastes (of diameter $250\text{-}280\mu\text{m}$) have been mostly affected by the scooping artifacts, which have a diameter around $50\text{-}80\mu\text{m}$. The used camera optics has a focal length 12mm and an aperture value 1.4 , viewing angle has been set to 45° , and the exposition time to $100\mu\text{s}$. During the inspections, the panels have lied on a moving conveyor belt with a speed of $0.5\text{-}1$

cm/s . The panel has been illuminated by nine light sources, arranged in a 9×9 array. Obtained images have 1024×768 resolution covering a $6\text{mm}\times 4.5\text{mm}$ PCB area (approximately $6\mu\text{m}/\text{pixel}$).

B. Recognition results

Some qualitative results of the hierarchical paste-scoop extraction are shown in Fig. 16. We have fulfilled the quantitative evaluation separately for the SP and SO objects, both at entity and pixel levels.

On one hand, we measure how many SPs and SOs are correctly or erroneously recognized in the different test sets, by counting the number of the True and False Positive, respectively True and False Negative entities in the detection results. Thereafter, entity level Recall (Rc) and Precision (Pr) rates are calculated, and the detection is characterized by the *F-score* [18], which is the harmonic mean of Rc and Pr (see SPOF and SOOF rows of Table II). On the other hand, we also investigate how accurate the extracted entity outlines are: we compare the resulting SP and SO “silhouette masks” to manually edited and verified Ground Truth masks, and calculate F-score of the pixel level detection (SPAF and SOAF in Table II). Finally, as one of the main purposes of prior interaction modeling in H^M MPP is to achieve improved SP alignment, we measured the average orientation errors of the rectangular and triangular Solder Pastes in the test images (SPOE in Table II).

As a baseline technique, we have used a morphology-based solution (*Morph*) introduced in [35] in details. In the *Morph* method, two thresholding operations are applied on the input image: the first one uses a lower threshold value, and results in the binary SP candidate mask. The second threshold enables us to extract the brightest image parts only which are supposed to contain the scoop center areas. Since bright SP parts also occur independently of scooping, a verification process is needed, which aims to remove false SO candidates. This post-processing step also ensures that each SP contains one scoop at most, which is a consequence of the manufacturing process.

Numerical evaluation results are shown in Table II. Concerning the extraction of the Solder Pastes, the object level rates (SPOF) are nearly perfect with both techniques, however at pixel (area) level (SPAF), the proposed H^M MPP method surpasses the *Morph* model with around 4.5%. Regarding the SP’s mean Orientation Error rate (SPOE) the difference is even more remarkable, as the H^M MPP outperforms *Morph* with an order of magnitude (1.36° vs. 10.78°), due to our proposed prior entity relation model part.

As for scooping investigation, the difference between the two methods is significant, as the proposed H^M MPP model outperforms the *Morph* technique by 21.6% at object level (see SOOF rate) and by 31.0% at pixel level (SOAF). Circuit technologists have confirmed, that based on our reported accuracy with H^M MPP a fair statistical analysis of the scooping effects can be performed for quality characterization of the solder joints in PCBs.

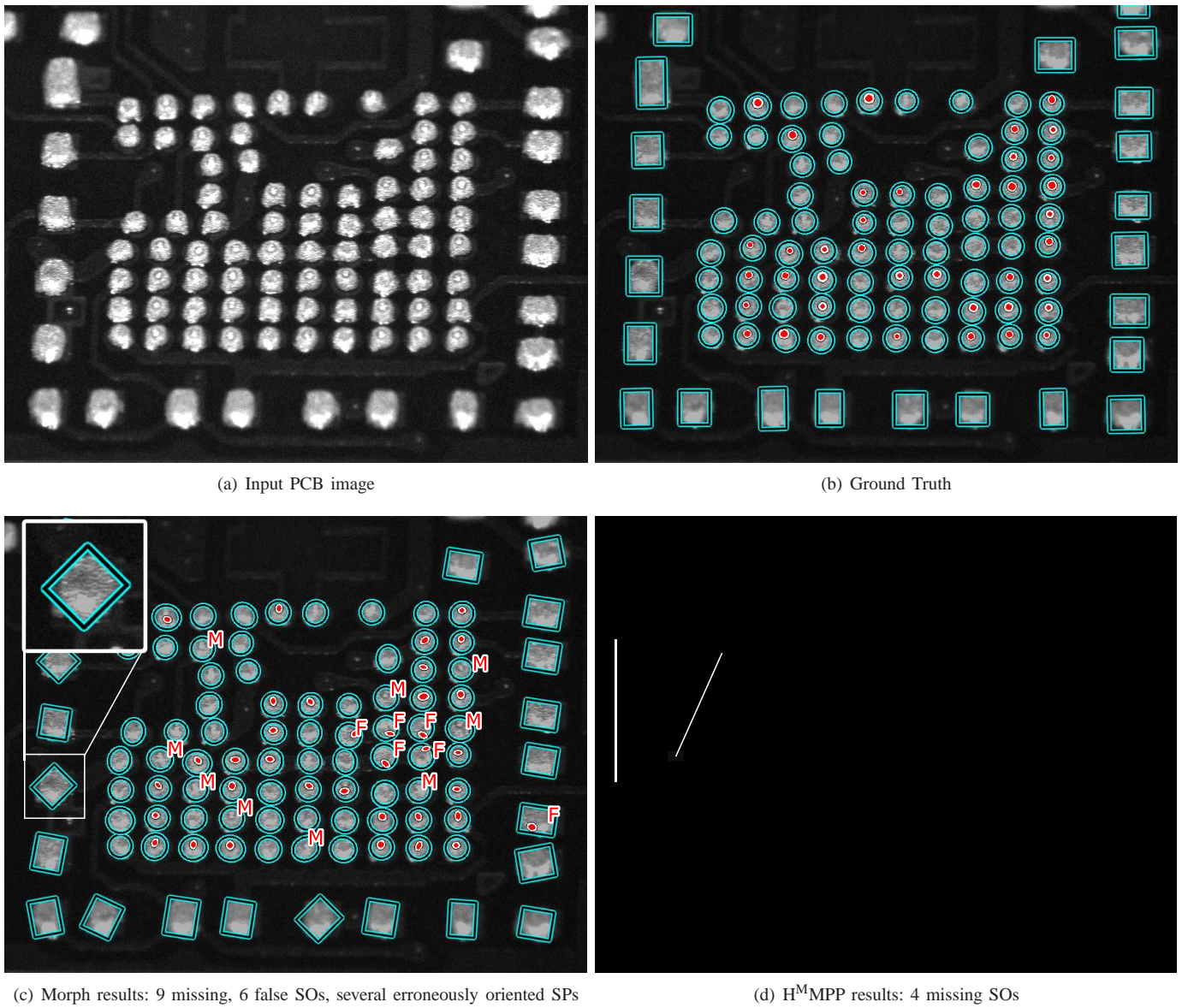


Fig. 16. Detection results of the proposed $H^M MPP$ method and comparison to the Ground Truth. F resp. M denote False resp. Missing scoops.

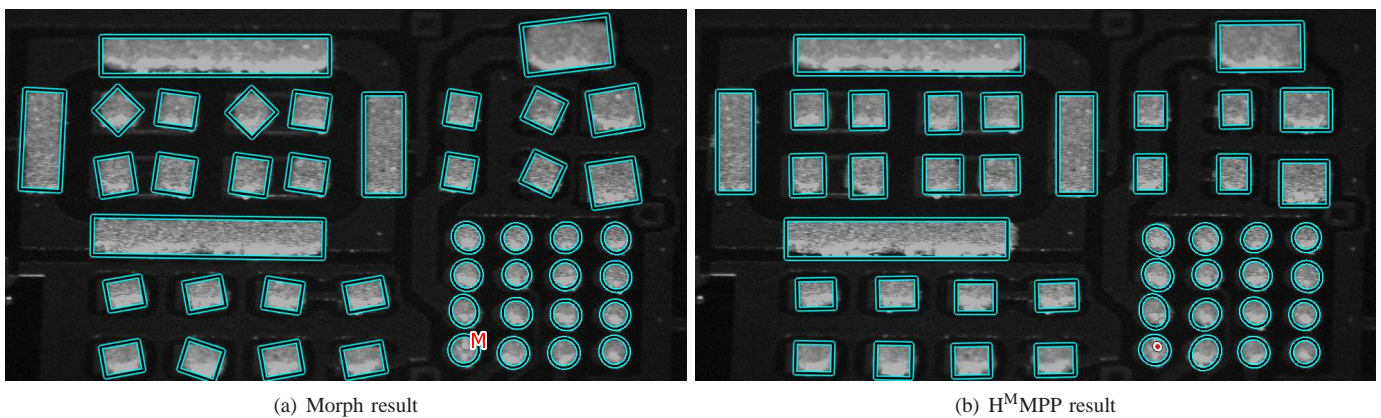


Fig. 17. Detection result in a circuit part with various element shapes and sizes. Morph results in a missing scoop and in several misaligned rectangles

TABLE II
PROPERTIES OF THE TEST SET AND RECOGNITION RESULTS WITH THE MORPH AND THE PROPOSED H^MMPP MODELS

	SetHeavy		SetSparse		SetDark		Overall	
Number of PCB images	44		66		15		125	
Total number of SPs	4655		4100		1283		10038	
Total number of SOs	664		122		0		786	
	<i>Morph</i>	H ^M MPP						
SP Obj. lev. F-rate (SPOF)	99.92%	99.96%	99.91%	99.97%	99.88%	99.88%	99.91%	99.96%
SP Area F-rate (SPAF)	88.84%	93.84%	90.12%	93.87%	88.43%	94.20%	89.44%	93.90%
SP Av. Orient Error (SPOE)	11.39°	1.83°	10.71°	1.01°	9.26°	1.59°	10.78°	1.36°
SO Obj. lev. F-rate (SOOF)	73.11%	92.29%	62.45%	92.94%	NA	NA	70.80%	92.40%
SO Area F-rate (SOAF)	51.46%	81.50%	53.88%	87.29%	NA	NA	52.01%	83.04%

C. Convergence speed of the HMBD optimization

To generate relevant SP candidates in the HMBD iterations, we have proposed a Bottom-up stochastic Entity Proposal (BEP) procedure in Sec. IV (see Fig. 12). As a consequence, the death step needs to deal with less inefficient circuit element candidates and high quality configurations can be reached more quickly. For evaluation, we compared the convergence speed of the HMBD optimization algorithm using the proposed BEP and the conventional Uniform Birth (UB) processes. In the UB case, the $\hat{P}_b(s)$ map follows a uniform distribution and the axis/side length and orientation parameters are also set as uniform random values. In Fig. 15, the SP Obj. lev. F-rate (SPOF) is shown as a function of the logarithm of the number of applied birth steps on a selected test image from the SetHeavy image set: The BEP approach reaches the final error rate with around thousand times less birth calls than the UB. Regarding other images and error rates, the observed tendencies were similar or even worst from point of view of the UB approach.

With the cooling parameter settings introduced in Sec. V, the computational time stayed tractable on the used test data sets: processing the 786 kPixel (1024×768) input images with 50-120 SP entities took around 5-15 sec. on a standard desktop computer (also depending on the scooping ratio). Since our test data providers confirmed that with their current technology, the stencil printing process takes around 15s for a four-piece batch of PCBs, with the current implementation of the H^MMPP model we can meet the real time verification requirement if we set four simultaneously working processing units. Note that for increasing the processing speed further, the MPP optimization algorithms can be parallelized and adopted for multiprocessor architectures [54].

VII. CONCLUSION

We have proposed a novel Hierarchical Multi Marked Point Process (H^MMPP) framework adopted to optical scooping analysis in PCBs. The method incorporates Solder Paste extraction and Scooping error detection in a joint probabilistic approach. An iterative optimization process extending the Multiple Birth and Death algorithm extracts the output configuration of Solder Pastes, considering the observed data and various prior interactions between the neighboring circuit elements. The accuracy is ensured by a Bayesian object model verification, meanwhile the computational cost is significantly decreased by a non-uniform stochastic object birth process,

which proposes relevant objects with higher probabilities based on low-level image features. Experiments confirmed the superiority of the proposed H^MMPP model and its usability for forthcoming industrial inspection systems. On the other hand, the methodological improvements of the paper over conventional MPP frameworks should later be adopted to various application areas, such as remote sensing or biological image analysis. Also in those domains, various objects appear in hierarchical parent-child relationship: for example, building roofs and chimneys in aerial photos, or biological cells and cell cores in microscopic images.

APPENDIX A

CHOOSING A PIXEL RANDOMLY INSIDE A SP ELLIPSE

In the *Child Maintenance step* of the HMBD algorithm, we need to choose internal points of SP objects randomly. This process is implemented in the following way. Let us consider a given SP ellipse $u = \{o_x, o_y, a_M, a_m, \theta, q_u\}$ and generate two random values $\tau, \varsigma \in [0, 1]$ according to uniform distribution. Using the general parametric equation of the ellipse, calculate $x(\tau, \varsigma)$ and $y(\tau, \varsigma)$ internal ellipse point coordinates:

$$x(\tau, \varsigma) = o_x + a_M \tau \cos(2\pi\varsigma) \cos \theta - a_m \tau \sin(2\pi\varsigma) \sin \theta$$

$$y(\tau, \varsigma) = o_y + a_M \tau \cos(2\pi\varsigma) \sin \theta + a_m \tau \sin(2\pi\varsigma) \cos \theta$$

the procedure returns the pixel with coordinates $x(\tau, \varsigma)$ and $y(\tau, \varsigma)$.

REFERENCES

- [1] K.-J. Choi, Y.-H. Lee, J.-W. Moon, C.-K. Park, and F. Harashima, "Development of an automatic stencil inspection system using modified hough transform and fuzzy logic," *IEEE Trans. Industrial Electronics*, vol. 55, no. 1, pp. 604 – 611, 2007.
- [2] C.-S. Cho, B.-M. Chung, and M.-J. Park, "Development of real-time vision-based fabric inspection system," *IEEE Trans. Industrial Electronics*, vol. 52, no. 4, pp. 1073–1079, 2005.
- [3] C.F. Hawkins, H.T. Nagle, R.R. Fritzscheier, and J.R. Guth, "The VLSI circuit test problem - a tutorial," *IEEE Trans. Industrial Electronics*, vol. 36, no. 2, pp. 111 – 116, 1989.
- [4] S. Khalaf, M. Zhu, P. Siy, and M. Abdelguerfi, "A real-time industrial pattern classification system," *IEEE Trans. Industrial Electronics*, vol. 36, no. 2, pp. 84–85, 1993.
- [5] W.E. Snyder, M.-L. Hsiao, K.J. Overton, and K.E. Boone, "Circuit board inspection using a range camera," *IEEE Trans. Industrial Electronics*, vol. 38, no. 2, pp. 142 – 149, 1991.
- [6] J.M. Reed and S. Hutchinson, "Image fusion and subpixel parameter estimation for automated optical inspection of electronic components," *IEEE Trans. Industrial Electronics*, vol. 43, no. 3, pp. 346 – 354, 1996.

- [7] H.H. Szu, "Automatic fault recognition by image correlation neural network techniques," *IEEE Trans. Industrial Electronics*, vol. 40, no. 2, pp. 197–208, 1993.
- [8] M. Moganti, F. Ercal, C.H. Dagli, and S. Tsunekawa, "Automatic PCB inspection algorithms: A survey," *Computer Vision and Image Understanding*, vol. 63, no. 2, pp. 287–313, March 1996.
- [9] B. Ionut, "Using mathematical morphology to detect the imperfections of the printed circuit boards," *Journal of Applied Computer Science & Mathematics*, vol. 2, no. 3, pp. 9–14, 2008.
- [10] P. Soille and P. Vogt, "Morphological segmentation of binary patterns," *Pattern Recogn. Lett.*, vol. 30, no. 4, pp. 456–459, 2009.
- [11] L-Z. Lin, L-S. Zhou, J-D. Wan, and Z-Q. Qian, "Study of PCB automatic optical inspection system based on mathematical morphology," in *International Conference on Computer Technology and Development*, Los Alamitos, CA, USA, 2009, vol. 2, pp. 405–408.
- [12] A. Kumar, "Computer-vision-based fabric defect detection: A survey," *IEEE Trans. Industrial Electronics*, vol. 55, no. 1, pp. 348–363, Jan. 2008.
- [13] S. Chen, G. Luo, X. Li, S. Ji, and B. Zhang, "The specular exponent as a criterion for appearance quality assessment of pearl-like objects by artificial vision," *IEEE Trans. Industrial Electronics*, 2011.
- [14] M.J. Ferreira, C. Santos, and J. Monteiro, "Cork parquet quality control vision system based on texture segmentation and fuzzy grammar," *IEEE Trans. Industrial Electronics*, vol. 56, no. 3, pp. 756–765, March 2009.
- [15] M. Chacon and S. Gonzalez, "An adaptive neural-fuzzy approach for object detection in dynamic backgrounds for surveillance systems," *IEEE Trans. Industrial Electronics*, 2011, In press.
- [16] A.N. Belbachir, M. Hofstätter, M. Litzengerger, and P. Schön, "High-speed embedded-object analysis using a dual-line timed-address-event temporal-contrast vision sensor," *IEEE Trans. Industrial Electronics*, vol. 58, no. 3, pp. 770–783, March 2011.
- [17] Yonghui Hu, Wei Zhao, and Long Wang, "Vision-based target tracking and collision avoidance for two autonomous robotic fish," *IEEE Trans. Industrial Electronics*, vol. 56, no. 5, pp. 1401–1410, May 2009.
- [18] C. Benedek, X. Descombes, and J. Zerubia, "Building development monitoring in multitemporal remotely sensed image pairs with stochastic birth-death dynamics," *IEEE Trans. Pattern Anal. Mach. Intell.*, vol. 34, no. 1, pp. 33–50, 2012.
- [19] O. Krammer and B. Sinkovics, "Improved method for determining the shear strength of chip component solder joints," *Microelectronics Reliability*, vol. 50, no. 2, pp. 235–241, 2010.
- [20] O. Krammer and Z. Illyefalvi-Vitéz, "Investigating the self-alignment of chip components during reflow soldering," *Periodica Polytechnica Electrical Engineering*, vol. 52, no. 1–2, pp. 67–75, 2008.
- [21] I. Fidan, R. P. Kraft, L. E. Ruff, and S. J. Derby, "Experiments to investigate the solder joint quality output of a prototype automated surface mount replacement system," *IEEE Trans. Components, Packaging, Manufacturing Technology*, vol. 21, no. 3, pp. 172–181, 1998.
- [22] J. Pan, G. L. Tonkay, R. H. Storer, and D. J. Leandri R. M. Sallade, "Critical variables of solder paste stencil printing for micro-bga and fine pitch QFP," in *Proc. IEEE/CPMT Int'l Electronics Manufacturing Technology Symposium*, 1999.
- [23] D. He, N. N. Ekere, and M. A. Currie, "The behavior of solder pastes in stencil printing with vibrating squeegee," *IEEE Trans. Components, Packaging, Manufacturing Technology*, vol. 21, no. 4, pp. 317–324, 1998.
- [24] S.C. Richard, "The complete solder paste printing processes," *Surface Mount Technology*, vol. 13, pp. 6–8, 1999.
- [25] Tsung-Nan Tsai, "Modeling and optimization of stencil printing operations: A comparison study," *Computers & Industrial Engineering*, vol. 54, no. 3, pp. 374–389, 2008.
- [26] P. Krippner and D. Beer, "AOI testing position in comparison," *Circuits Assembly*, pp. 26–32, 2004.
- [27] S.H. Mannan, N.N. Ekere, E.K. Lo, and I. Ismail, "Predicting scooping and skipping in solder paste printing for reflow soldering of SMT devices," *Soldering & Surface Mount Technology*, vol. 5, no. 3, pp. 14–17, 1993.
- [28] H. Xu, M. Li, J. Kim, and D. Kim, "Local melting and shape controlling of solder joint via induction heating," *Journal of materials processing technology*, vol. 209, no. 6, pp. 2781–2787, 2009.
- [29] X.J. Fan, B. Variaand, and Q. Han, "Design and optimization of thermo-mechanical reliability in wafer level packaging," *Microelectronics Reliability*, vol. 50, no. 4, pp. 536–546, 2010.
- [30] O. Nousiainen, L. Lehtiniemi, T. Kangasvieri, R. Rautioaho, and J. Vahakangas, "Thermal fatigue endurance of collapsible 95.5Sn4Ag0.5Cu spheres in LTCC/PWB assemblies," *Microelectronics Reliability*, vol. 48, no. 4, pp. 622–630, 2008.
- [31] Y. Takagi, S. Hata, and S. Hibi, "Visual inspection machine for solder joints using tiered illumination," in *SPIE Machine Vision Systems Integration in Industry*, 1990, vol. 1386, pp. 21–29.
- [32] M.T. Holzmann, "Automatic optical inspection of circuit assemblies in a high mix/low volume environment," in *Proc. of the Surface Mount Techn. Assoc.*, 2004.
- [33] H.J. Tahir, N. Parry, A. Pallikaris, and I.J. Murray, "Higher-order aberrations produce orientation-specific notches in the defocused contrast sensitivity function," *Journal of Vision*, vol. 9, no. 7, pp. 1–12, 2009.
- [34] Y.-W. Tai and M.S. Brown, "Single image defocus map estimation using local contrast prior," in *IEEE International Conference on Image Processing*, Piscataway, NJ, USA, 2009, pp. 1777–1780, IEEE Press.
- [35] C. Benedek, "Detection of soldering defects in printed circuit boards with hierarchical marked point processes," *Pattern Recogn. Letters*, vol. 32, no. 13, pp. 1535–1543, 2011.
- [36] J. Sauvola and M. Pietikäinen, "Adaptive document image binarization," *Pattern Recognition*, vol. 33, pp. 225–236, 2000.
- [37] L. Vincent, "Morphological grayscale reconstruction in image analysis: Applications and efficient algorithms," *IEEE Trans. on Image Processing*, vol. 2, pp. 176–201, 1993.
- [38] M. Moganti and F. Ercal, "Segmentation of printed circuit board images into basic patterns," *Computer Vision and Image Understanding*, vol. 70, no. 1, pp. 74–86, April 1998.
- [39] L. Vincent and P. Soille, "Watersheds in digital spaces: an efficient algorithm based on immersion simulations," *IEEE Trans. Pattern Anal. Mach. Intell.*, vol. 13, no. 6, pp. 583–598, 1991.
- [40] C.J. Chen, S.H. Lai, S.W. Liu, T. Ku, and S.Y.C. Yeh, "Optical pcb inspection system based on hausdorff distance," *Machine Vision Applications in Industrial Inspection*, vol. 5679, pp. 53–61, 2005.
- [41] A.A. Rodriguez and J.R. Mandeville, "Image registration for automated inspection of printed circuit patterns using CAD reference data," *Machine Vision and Applications*, vol. 6, no. 4, pp. 233–242, 1993.
- [42] C. S. Chen, C. W. Yeh, and P. Y. Yin, "A novel fourier descriptor based image alignment algorithm for automatic optical inspection," *Journal of Visual Communication and Image Representation*, vol. 20, no. 3, pp. 178–189, April 2009.
- [43] J.L.C. Sanz and A.K. Jain, "Machine-vision techniques for inspection of printed wiring boards and thick-film circuits," *J. Opt. Soc. Am. A*, pp. 1465–1482, 1986.
- [44] X. Descombes and J. Zerubia, "Marked point processes in image analysis," *IEEE Signal Processing Magazine*, vol. 19, no. 5, pp. 77–84, September 2002.
- [45] S. Geman and D. Geman, "Stochastic relaxation, Gibbs distributions and the Bayesian restoration of images," *IEEE Trans. Pattern Analysis and Machine Intelligence*, vol. 6, no. 6, pp. 721–741, 1984.
- [46] M. Ortner, X. Descombes, and J. Zerubia, "A marked point process of rectangles and segments for automatic analysis of digital elevation models," *IEEE Trans. Pattern Anal. Mach. Intell.*, vol. 30, no. 1, pp. 105–119, 2008.
- [47] X. Descombes, R. Minlos, and E. Zhizhina, "Object extraction using a stochastic birth-and-death dynamics in continuum," *J. Math. Imaging and Vision*, vol. 33, pp. 347–359, 2009.
- [48] F. Chatelain, X. Descombes, and J. Zerubia, "Parameter estimation for marked point processes. application to object extraction from remote sensing images," in *Energy Minimization Methods in Computer Vision and Pattern Recognition (EMMCVPR)*, Bonn, Germany, 2009.
- [49] C. Benedek, "Analysis of solder paste scooping with hierarchical point processes," in *Proc. IEEE International Conference on Image Processing (ICIP)*, Brussels, Belgium, Sept. 2011.
- [50] F. Lafarge, G. Gimel'farb, and X. Descombes, "Geometric feature extraction by a multi-marked point process," *IEEE Trans. Pattern Analysis and Machine Intelligence*, vol. 32, no. 9, pp. 1597–1609, September 2010.
- [51] Z. Tu and S-C. Zhu, "Image segmentation by Data-Driven Markov Chain Monte Carlo," *IEEE Trans. Pattern Anal. Mach. Intell.*, vol. 24, pp. 657–673, 2002.
- [52] C. Benedek, T. Szirányi, Z. Kato, and J. Zerubia, "Detection of object motion regions in aerial image pairs with a multi-layer Markovian model," *IEEE Trans. on Image Processing*, vol. 18, no. 10, pp. 2303–2315, 2009.
- [53] Á. Utasi and C. Benedek, "A 3-D marked point process model for multi-view people detection," in *IEEE Conf. Computer Vision and Pattern Recognition (CVPR)*, Colorado Springs, USA, 2011, pp. 3385–3392.
- [54] N. Bambos and S. C. Chen, "Optimality aspects of greedy schemes in parallel processing of random graph-structured jobs," *Probability in the Engineering and Informational Sciences*, vol. 8, pp. 229–243, 1994.